JTTEE5 19:11–23
DOI: 10.1007/s11666-009-9414-2
1059-9630/$19.00 © ASM International

The Role of Substrate Surface Chemistry on Splat Formation During Plasma Spray Deposition by Experiments and Simulations

A.T.T. Tran and M.M. Hyland

(Submitted April 25, 2009; in revised form August 16, 2009)

NiCr single splats were plasma-sprayed on aluminum and stainless steel substrates, which were modified by immersion in boiling water, to grow specific types of oxide/oxyhydroxide on the surface. It was observed that there was no splat formation on aluminum substrate. In contrast, a significant number of splats were formed on stainless steel substrate. The differences in splat formation on aluminum and stainless steel surfaces corresponded to the variations of thickness and proportions of the oxide/oxyhydroxide layer on the surfaces. A three-dimensional numerical model was developed to simulate the impact of a droplet onto the substrate. The simulation illustrated good agreement with experimental observations. The effect of the oxide layer on the splat morphology was also examined. It was suggested that the splat morphology was more strongly influenced by water release from the dehydration of oxyhydroxide to oxide rather than by simple presence of the oxide layer on the substrate surface.

Keywords FEM, numerical modeling, oxyhydroxide, surface chemistry, water desorption

1. Introduction

Plasma spray technology has been widely employed for deposition of engineering coatings. Coatings produced with customized surface properties are used for a variety of industrial applications. Fundamentally, the coatings are formed as the molten particles impact and spread out to form overlapping splats. Thus, the performance of the coatings is closely linked with the way the individual splats are formed. The layered microstructure and splat-substrate bonding are profoundly affected by the spraying conditions, substrate surface, and the particle conditions (Ref 1, 2). During the last decade, many papers have demonstrated that splat morphology and behavior in plasma spray strongly depend on substrate temperature (Ref 1-11). Such works showed that substrates heated above a given temperature, (defined as the transition temperature by Fukumoto (Ref 12) gave rise to favorable, disk-shaped splats. In contrast, splats on substrates held

This article is an invited paper selected from presentations at the 2009 International Thermal Spray Conference and has been expanded from the original presentation. It is simultaneously published in *Expanding Thermal Spray Performance to New Markets and Applications: Proceedings of the 2009 International Thermal Spray Conference*, Las Vegas, Nevada, USA, May 4-7, 2009, Basil R. Marple, Margaret M. Hyland, Yuk-Chiu Lau, Chang-Jiu Li, Rogerio S. Lima, and Ghislain Montavon, Ed., ASM International, Materials Park, OH, 2009.

A.T.T. Tran and **M.M. Hyland**, Chemical & Materials Engineering Department, The University of Auckland, Private Bag 92019, Auckland, New Zealand. Contact e-mail: atra021@aucklanduni.ac.nz.

Nomenclature

B	body force
C_p	specific heat capacity
f	mass fraction
F	volume of fraction of the droplet
k	thermal conductivity
L	latent heat of fusion
n	interface normal vector pointing from the droplet to air
R_c	thermal contact resistance at the droplet-substrate interface
T	temperature
T_0	substrate initial temperature
T_m	equilibrium melting temperature
p	pressure
t	time
u	velocity vector
α	thermal diffusivity
ρ	density
μ	effective viscosity
σ	surface tension coefficient
κ	surface curvature
δ	interface delta function
l	liquid phase
m	equilibrium melting temperature
ox	oxide
s	solid
sub	substrate
α	droplet
β	air

below the transition temperature were predominantly irregular or splashed shaped (Ref 6-8, 11-13). Splashing and disintegration of the splat have been proposed to be caused by the release of adsorbates from the substrate surface (Ref 7, 8). When the droplet impacts the substrate at high temperature, desorption of adsorbates from the substrate surface occurs, forming a gas barrier between the splat and substrate and disrupting the splat formation process. There has been some debate about the nature of the adsorbates, and whether or not it is the adsorbate release or the oxide roughness changes that are responsible. By examining the splat formation of NiCr particles on both aluminum and stainless steel substrates which were modified by thermal and hydrothermal treatments, our previous results (Ref 14) showed that the 'adsorbate' responsible for disrupting splat formation is in fact water physisorbed and chemisorbed on the oxide. The release of water due to the dehydration of surface oxyhydroxide (chemisorbed water) to oxide and the formation of thick oxide/oxyhydroxide layer impeded the spreading and adhesion of the splat, which induced the splashing ability of the splat. This effect dominated over surface morphology changes. The release of water vapor reduces the physical contact between the splat and substrate reduced. The splat spreads on the gas barrier to a very thin sheet and then easily broken up (Ref 11, 13). Heating the substrate can remove the adsorbed water prior to spraying, resulting in improved physical contact between the splat and substrate which enhanced the formation of disk-splats (Ref 7, 8, 14).

Along with substantial experimental studies that have been carried out, three-dimensional numerical models have been developed to understand the splat spreading and solidification mechanism (Ref 4, 13, 15-17). Modeling shows that splat morphology is strongly dependent on thermal contact resistance which accounts for discontinuity at the interface between splat and substrate (Ref 13, 17-19). Bussmann et al. (Ref 20, 21) developed a three-dimensional model using volume tracking method to simulate water droplets falling with low velocity (~1 m s^{-1}) and to study the splash of a droplet on a solid surface. However, heat transfer and phase change during droplet impact was not considered in these models. Pasandideh et al. (Ref 13, 17) extended the model of Bussmann et al. (Ref 20, 21) to include heat transfer and solidification to simulate the droplet impact and solidification onto a flat surface. By comparing the splat shape from the experimental results and simulations, Pasandideh et al. (Ref 13) proposed that heating the substrate produced an oxide layer which increased thermal contact resistance and prevented the splashing at the splat rim due to the solidification front. However, they did not explore the relation between the oxide thickness and the degree of splashing. In contrast, Cedelle et al. (Ref 22) and Bahbou et al. (Ref 16) proposed that thermal contact resistance significantly decreased on the oxidized smooth surface compared to the non-oxidized one due to the growth of nano-structured oxides. The reduction of thermal contact resistance resulted in a better contact between splat and substrate (Ref 13, 16, 22). Another explanation is that the oxidized surface contained less adsorbate than the non-oxidized, thus enhancing splat/substrate contact and reducing thermal contact resistance (Ref 7), promoting wetting and avoiding splashing (Ref 9). McDonald et al. have recently (Ref 23) suggested that neither surface roughness nor oxide layer can completely explain the decrease of thermal contact resistance with surface heating. The evaporation of adsorbates from the substrate surface which create a barrier film appears to be the main factor. In addition, our recent experimental results (Ref 14) have confirmed that a change of the chemical structure of the oxide and oxyhydroxide layer on the substrate surface correlated with the splat morphology. Although the experimental evidence points to surface chemistry playing a role, most models have focused on the effect of surface roughness (Ref 23-25) on splat morphology and neglected the effect of oxide layer thickness and gas release. Thus, in this study, NiCr splats were deposited on stainless steel and aluminum substrates subjected to pretreatments designed to grow specific types of oxides on the surface. The collected splats were examined to determine the correlation between the splat formation and the substrate surface chemistry. A three-dimensional numerical model was developed using commercial Ansys CFX to simulate the splat impact involving the effect of oxides thickness on splat morphology. From the experiments and simulations, the role of substrate surface chemistry on splat formation during plasma spray deposition can be clarified.

2. Experimental Details

In this work, commercial polished aluminum 5052 and stainless steel 304 substrates were hydrothermally treated by immersion in boiling de-ionized water for 30 min (referred to as "Al_B" and "SS_B," respectively, in this article). The samples were then patted dry with paper towels and stored in a dessicator to preserve the surface chemistry until they were ready to be sprayed. The samples were sprayed within 1 day of pretreatment. The time between removing from the dessicator and spraying was less than 60 min. Al_B and SS_B samples were thermally sprayed at the same time with Ni20Cr alloy powder ($-45+5$ μm, Sulzer Metco 43VF-NS, Switzerland) employing plasma spray technique under atmospheric conditions. Plasma spraying was carried out with a Sulzer Metco (USA) 7MB gun operating at a current of 550 A and a voltage of 74 V. The spraying distance between the gun and the substrate was kept at 80 mm. The powder was injected at a feed rate of 1 g min^{-1}. The plasma gas mixture was argon and hydrogen, at a flow rate of 47.6 and 5.4 SLPM, respectively. Collected splats on the ($25 \times 25 \times 3$ mm) substrate were characterized qualitatively and quantitatively using a Philips FEGXL30 scanning electron microscope (SEM) and ImageJ imaging software (National Institute of Health, Washington DC, USA). Back scattered images were used to distinguish between splat and substrate. Five images at a magnification

of 150 times were acquired at random locations for image analysis, with at least 50 splats each image. The obtained information included Feret diameter, circularity, area, and perimeter of individual splats. The Feret diameter is the longest distance between any two points on the boundary of the splat. A value of circularity of 1 represents to a perfect circle: the closer to zero, the more elongated the splat. The splat-substrate interfaces were investigated with a FEI xP200 Focused Ion Beam (FIB) microscope.

3. Numerical Model

The impact of a molten droplet on the substrate was modeled using a free surface model in which the fluids (droplet and air) are separated by a distinct resolvable interface. At the interface between the droplet and surrounding air, the surface tension, which was based on the Continuum Surface Force model (CSF) of Brackbill et al. (Ref 26), was modeled as a volume force concentrated at the interface. As a molten droplet impacts the colder substrate, the droplet temperature rapidly decreases. Once the droplet temperature reaches the melting temperature, phase change from liquid to solid occurs. Because heat transfer due to convection and radiation are much smaller than conduction, they are not included in the model (Ref 13, 27). Thus, the temperature distribution of substrate and droplet during droplet spreading and cooling is obtained using a transient heat conduction model. The following assumptions were made to model the present problem mathematically:

- The liquid flow was incompressible and laminar,
- The effect of ambient air during droplet impact was negligible,
- The velocity of the solid phase is zero,
- Tangential stresses at the free surface and gravitational force were neglected,
- No slip and no penetration boundary conditions were applied at the substrate surface,
- The energy source and the viscous dissipation were neglected,
- Thermal contact resistance and surface tension were constant,
- The physical properties of the droplet and substrate were constant.

Taking into account the above assumptions, the equations of mass, momentum, and energy conservation for the binary solid-liquid phase change system of an incompressible droplet are presented as below. Full details are described elsewhere (Ref 28-30) and need not be repeated here.

Mass conservation

$$\nabla \cdot u = 0 \qquad \text{(Eq 1)}$$

Momentum conservation

$$\rho \frac{\partial u}{\partial t} + \rho \nabla \cdot (uu) = -\nabla p + \nabla \cdot \left(\mu_l \frac{\rho}{\rho_l} \nabla u \right) + \rho B \qquad \text{(Eq 2)}$$

Energy conservation

$$\frac{\partial T}{\partial t} + \nabla \cdot (uT) = \alpha \nabla \cdot (\nabla T) + S_h \qquad \text{(Eq 3)}$$

where the source term

$$S_h = -\frac{L}{C_{pl}} \frac{\partial f_l}{\partial t} + \frac{C_{pl} - C_{ps}}{C_{pl}} \frac{\partial}{\partial t}(f_s T) \qquad \text{(Eq 4)}$$

The relationship between droplet temperature and liquid mass fraction is given by:

$$f_l = \frac{C_{pl}}{L}(T - T_m) \qquad \text{(Eq 5)}$$

The liquid and solid mass fraction is constrained to unity, that is:

$$f_l + f_s = 1 \qquad \text{(Eq 6)}$$

The interface between the droplet and air fluids, the shape and trajectory of the droplet were tracked using the ''volume of fraction'' method (Ref 30). The volume of fraction of the droplet (F) specifies the fraction of the volume of each computational cell in the grid occupied by the droplet and is defined to be unity for all the points inside the droplet and zero elsewhere. A value of F between 0 and 1 represents the interface between the droplet and air. The volume of fraction of droplet for a given flow is determined by the passive transport equation:

$$\frac{\partial F}{\partial t} + \nabla u F = 0 \qquad \text{(Eq 7)}$$

Due to the small size of the droplet, gravitational forces were neglected in this study. Thus, surface tension is the dominant force contributing to body force governing the droplet behavior. The surface tension force per unit interface area given by Continuum Surface Force model is (Ref 26):

$$F_{\alpha\beta} = -\sigma \kappa_{\alpha\beta} n_{\alpha\beta} \delta_{\alpha\beta} \qquad \text{(Eq 8)}$$

where α and β represent the droplet and air, respectively; σ is the surface tension coefficient; κ is the surface curvature, taken negative if the center of curvature is in air; $n_{\alpha\beta}$ is the interface normal vector pointing from the droplet to air which is calculated from the smoothed volume of fraction; $\delta_{\alpha\beta}$ is the interface delta function which is zero away from the interface to ensure that the surface tension force is only active near to the interface.

Heat transfer between the droplet and substrate was assumed to be due to heat conduction alone. A thermal contact resistance (R_c) is used to account for discontinuity at the interface between the droplet and the substrate:

$$\frac{1}{R_c}(T - T_{sub}) = k \frac{\partial T}{\partial x} \qquad \text{(Eq 9)}$$

Since there is no flow inside a solid phase, the heat conduction equation through the substrate is written as:

$$\frac{\partial T_{sub}}{\partial t} = \alpha_{sub} \nabla^2 T_{sub} \quad \text{(Eq 10)}$$

In this study, the commercial finite element code CFD package Ansys CFX version 11 was used to model the solidification and spreading of droplet on the substrate. The governing equations are represented discretely in unstaggered, collocated grids and solved by an algebraic multi-grid solver for each control volume (Ref 31). An approximation of the value of each variable at specific points throughout the domain can then be obtained. In this method, all variables are computed and stored at the same geometrical location. Thus, the data structure is quite simple. In addition, Rhie-Chow interpolation is used to avoid pressure-velocity decoupling. As a result, CFX solves all conservation equations in one linear system, with all equations being fully coupled, which makes the solver more robust and enhances the accuracy. However, the principal drawbacks of CFX are the high storage needed for all the coefficients and the limited memory during the run (Ref 32).

Further details about the numerical discretization of the governing equations can be found in the Ansys manual (Ref 32). However, the general solution algorithm for each time step is summarized as follows:

1. Determine the fluid topology by updating all the volume of fraction functions (F). The volume of fraction of fluid is defined by solving Eq 7 through the step function using VOF tracking method (Ref 30).
2. Interpolate to get the interface normal vectors and the surface curvature from the volume of fraction using the CSF model (Ref 26).
3. Obtain the body force from Eq 8.
4. Solve the mass and momentum equations (Eq 1 and 2) to get the coupled value of pressure and velocity field.
5. Solve implicit energy conservation for the droplet temperature (Eq 3 and 4) with given liquid mass fraction (f_l) and calculated velocity.
6. Update value of liquid mass fraction from Eq 5.
7. Update the liquid-solid boundary after a given time period based on liquid and solid mass fraction.
8. Solve Eq 9 for substrate surface temperature.
9. Solve heat conduction Eq 10 in substrate to get substrate temperature distribution.

A rectangular free surface domain for the droplet was made to be $8r \times 8r \times 2.1r$ (where r is initial radius of droplet). The length of the substrate was chosen to ensure that the bottom substrate temperature is constant at 25 °C. Initial average temperature and velocity of the droplet, which were measured using DPV-2000 system (Tecnar, Canada), were 2527 °C and 130 m s^{-1}, respectively. The initial temperature of 2527 °C of the droplet was chosen to ensure that droplets were fully molten at the impact.

Heat transfer equations with a phase change induced by inter-phase heat transfer in the interior of the flow were incorporated into the program using a multiphase Eulerian-Eulerian grid model. A homogeneous binary mixture of solid and liquid undergoing phase change with melting temperature was used as a property of the droplet. The latent heat of fusion was indirectly obtained as the difference between static enthalpies of the two phases at the selected melting point and reference pressure of 10^5 Pa. Only a 1/4 domain was modeled to reduce processing time. Symmetry boundary conditions were applied to two new boundaries. Adiabatic boundary conditions were used at the droplet-free surface (Fig. 1a). The physical properties of nickel droplet and aluminum substrate are tabulated in Table 1. To improve the accuracy and stability of solution, a uniform of hexagonal mesh was used. Mesh size was set to 20 meshes for droplet radius. The same mesh size was applied for substrate domain.

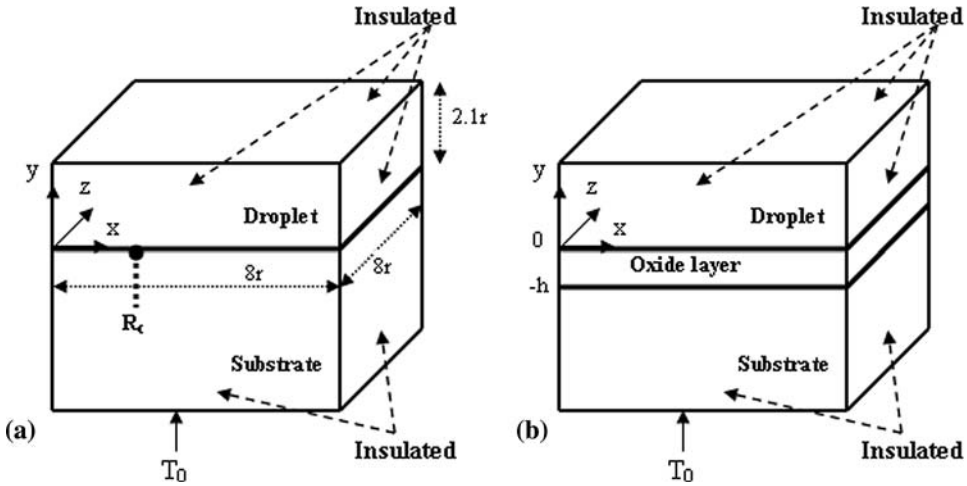

Fig. 1 Schematic of the droplet on substrate (a) with thermal contact resistance (R_c) at the droplet-substrate interface, (b) including oxide layer in between the droplet and substrate

Table 1 Physical properties of splat and substrate used in the simulation

Physical properties	Ni (Ref 41)	SS (Ref 41)	Al (Ref 41)	Al_2O_3 (Ref 41)	Unit
Initial temperature	2427	25	25	25	°C
Initial velocity	110				m s^{-1}
Melting point temperature	1453	1450			°C
Surface tension	1.78				N m^{-1}
Viscosity	3.3×10^{-3}				Pas
Latent heat of fusion	2.9×10^{5}				J kg^{-1}
Thermal conductivity of liquid	43				W m^{-1} K^{-1}
Thermal conductivity of solid	80	28	238	17	W m^{-1} K^{-1}
Specific heat capacity of liquid	620				J kg^{-1} K
Specific heat capacity of solid	595	690	984	780	J kg^{-1} K
Density of liquid	7,780				kg m^{-3}
Density of solid	8,450	7,854	2700	3500	kg m^{-3}
Thermal diffusivity		5.17×10^{-6}	8.95×10^{-5}	6.2×10^{-6}	m^2 s^{-1}

A very small time step of 0.5 ns was initially set to obtain good convergence and domain imbalance (below 0.1%).

4. Results and Discussion

4.1 Splat Characterization

Collected splats were analyzed using SEM and ImageJ imaging software to obtain quantitative and qualitative information on splat morphologies. A typical image of splat formation on SS_B surface is shown in Fig. 2(a). Splats were classified as either disk-type splats or splash splats. In addition, these splat types were divided into two subcategories: round (Fig. 2b) and donut splats (Fig. 2c), round (Fig. 2d) and irregular splash splats (Fig. 2e). Round disk splats are here defined as splats whose central pore diameter was smaller than 4 μm. Donut splats are defined as a round disk splat with a central pore larger than 4 μm in diameter. Round splash splats are smaller, more irregular circumference fingers. It was observed that most of the disk or donut splats exhibited a similar characteristic: a reasonably round shape with few small fingers, a flat surface, micro-pores, central pore, and a distinct curled up splat rim. From the image analysis, it was found that there were 43%, 20%, 2%, and 35% of round disk splats, donut disk splats, round splash splats, and irregular splash splats, respectively. The disk splats were found to have an average diameter of ~44.2 μm and a circularity of ~0.72 (Fig. 3). However, the donut disk splat exhibited a larger diameter (~56.9 μm) and a more circular shape (~0.79). Assuming that the average initial diameter of the droplet was 25 μm, the average flattening ratio ranged from 1.8 to 2.2 approximately.

The interfaces between splats and the SS_B substrate were carefully examined for each splat type using FIB. Figure 4(a) is the SEM image of the donut splat prior to cross sectioning. Figure 4(b) shows the cross section FIB image across the central pore of the same splat. A platinum strip was deposited on the top of the splat surface to protect the specimen surface against the beam damage during milling. It was observed that the splat was in good contact with the substrate. A large portion of porous oxide (1) was found at the central pore of the splat. Oxide was also formed as a thin layer at the outer surface and accumulated at the periphery of the splat. Micro pores (2) were found at the interface. Other cross sections were performed across the periphery (Fig. 4d) of the round disk splat (Fig. 4c). A high degree of delamination (3) away from the substrate at the splat periphery was observed. The average splat thickness ranged from 1 to 2 μm. More importantly, the FIB image (Fig. 4d, e) indicates a local area at the splat-substrate interface where there was apparent jetting with a length of approximately 1 μm of the substrate into the splat to form the interlock structure as shown in the Fig. 4(e). The degree of contact between the splat and the substrate was very high at this location.

Several cross section FIB images were taken and examined. Overall, almost all disk splats on boiled stainless steel substrate exhibited similar common features: delamination at the periphery, micro-pores at the interface, oxide formation at the central pore, at the outer surface and at the periphery of the splat, and the diffusion/jetting of the substrate into the splat at some specific locations near the central of the splat. The NiCr splat was generally in very good contact with the substrate at these locations. The diffusion/jetting of the substrate toward the NiCr splat indicated the phenomenon of substrate melting. However, the characterization of substrate melting was not in the scope of this article. More details of substrate melting can be found in other article (Ref 33).

To allow for direct comparison of the splat formation, SS_B and Al_B surfaces were sprayed at the same time. A significant number of splats with the density of 75 splats per mm^2 were formed on SS_B surface. In contrast, there was no splat formation on Al_B surface. Instead, evidence of splat residue, such as scattered fine droplets and impact marks were found on the surface as in Fig. 5.

It is well known that splat formation and splat morphology depended on spraying conditions, particle properties, and substrate surface conditions (Ref 1, 2). Thus, to study the effect of those parameters on splat formation on Al_B surface, nickel particles were also sprayed on Al_B surface at different particle velocities and temperatures. Again, no splats were found. This is consistent with previous results where no NiCr splat formation occurred on hydrothermally treated aluminum

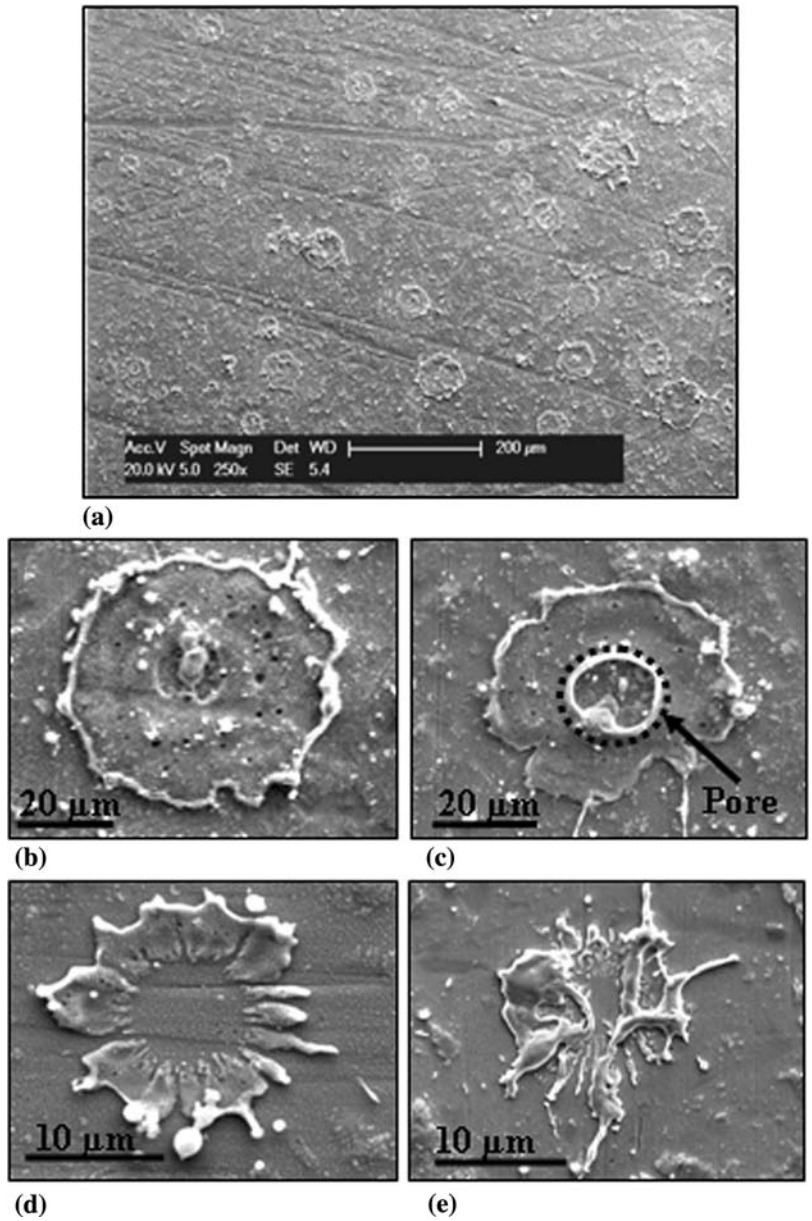

Fig. 2 (a) Typical images of collected splats on the SS_B surface, (b) round disk splat, (c) donut splat, (d) round splash splat, and (e) irregular splash splat

(c.f. Al_B surfaces here) using HVAF spraying (Ref 34), suggesting that splat formation on Al_B surface was dependent on neither spraying parameters nor particle properties. Our previous study (Ref 14) also confirmed that surface roughness did not contribute to the splat formation on Al_B surface. Thus, the absence of splat formation on Al_B surface is almost certainly due to the substrate surface chemistry.

The surface chemistry of Al_B and SS_B was studied using XPS. Wide scans and narrow scans were collected. For the SS_B, narrow scans of O 1s (Fig. 6a) and Fe 2p (Fig. 6b) were used to determine the oxidation state of each element. The O 1s peak was resolved into three different photopeaks representing the oxide (O^{2-}, 530 ± 0.1 eV), oxyhydroxide (OH^-, 531.3 ± 0.1 eV), and adsorbed $OH^{-\delta}$ (532.1 ± 0.1 eV) (Fig. 6a) (Ref 35). The proportion of oxyhydroxide was estimated at about 41%. The Fe 2p3/2 envelop was fitted using Gupta-Sen multiplet peaks (Ref 35) in which the oxide peak was further divided into two different peaks: Fe^{2+} and Fe^{3+} (Fig. 6b). The oxide layer was estimated at 4.2 nm thick based on the equation in the literature (Ref 35, 36). The film layer included a thin layer of oxyhydroxide at the outermost surface, followed by an oxide layer with the total thickness of 4.2 nm on the SS_B substrate. Oxyhydroxide was also observed on the surface of Al_B (Fig. 6c). However, the proportion and thickness of oxyhydroxide on Al_B was significant difference compared to SS_B

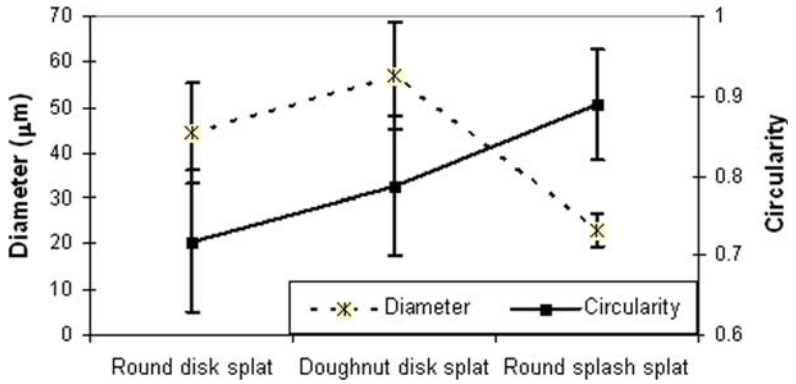

Fig. 3 Average diameter and circularity of the splats on the SS_B surface

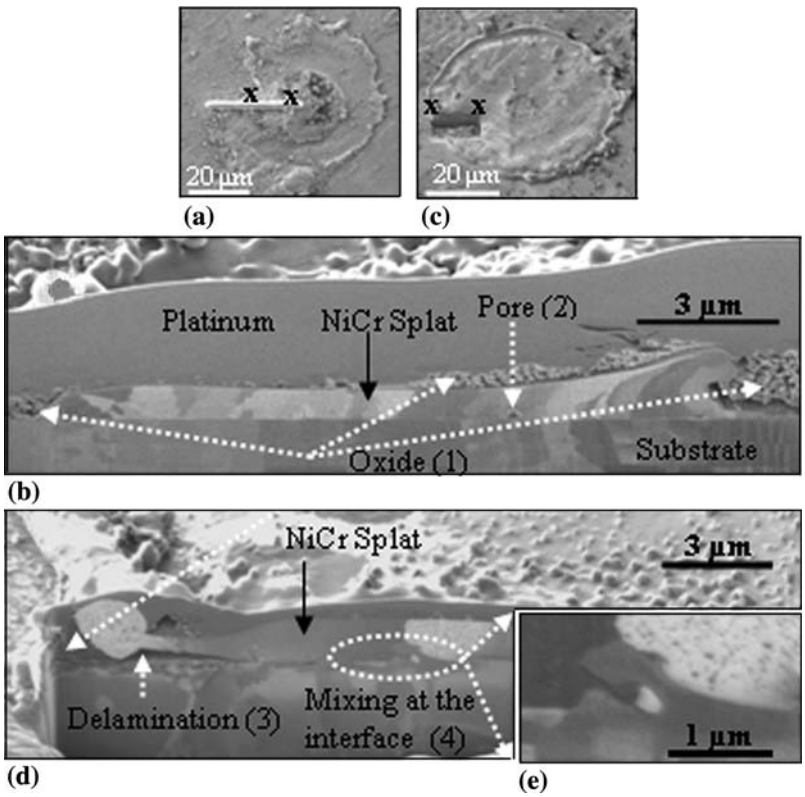

Fig. 4 Cross-sectional FIB images of NiCr splats: (a, b) across the central pore of the splat, (c, d) across the edge of the splat, and (e) enlargement of the jetting of the substrate to the splat

surface. The Al_B sample had equal proportions of oxide and oxyhydroxide. In addition, the absence of metal peak in Al 2p (Fig. 6d) confirmed that the oxide/oxyhydroxide layer formed on Al_B surface was larger than the XPS depth (8 nm). Thus, the oxide layer thickness on Al_B was analyzed by two ion beam techniques, Rutherford Backscattering Spectroscopy (RBS) and Elastic Recoil Detection Analysis (ERDA). The results from RBS and ERDA showed that Al_B surface had a 226 nm thick layer on the outer surface with a composition of AlOOH and a further 66 nm thick aluminum oxide layer diffusing into the substrate. It was also found that the chromium content on the SS_B surface increased compared to prior to hydrothermal treatment. Thus, it is possible that the enrichment of a chromium-rich oxide on the SS_B surface protected the surface out of further oxidation, resulting in a major difference in surface oxide/oxyhydroxide thickness on boiled stainless steel and aluminum.

The oxide/oxyhydroxide thickness on Al_B was several orders of magnitude larger than that on SS_B, resulting in a significant difference in surface topology between two

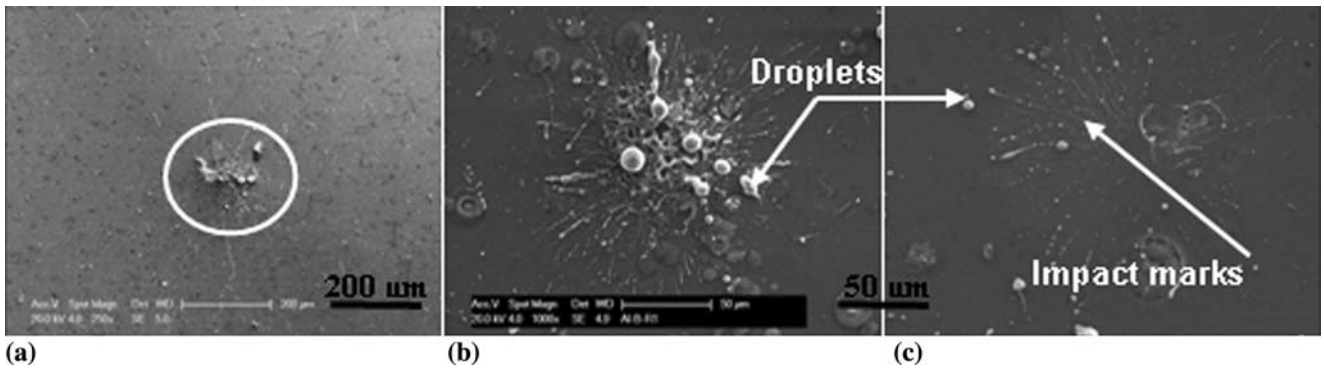

Fig. 5 (a) Typical image of splashing on the Al_B surface, (b) droplet, and (c) impact marks

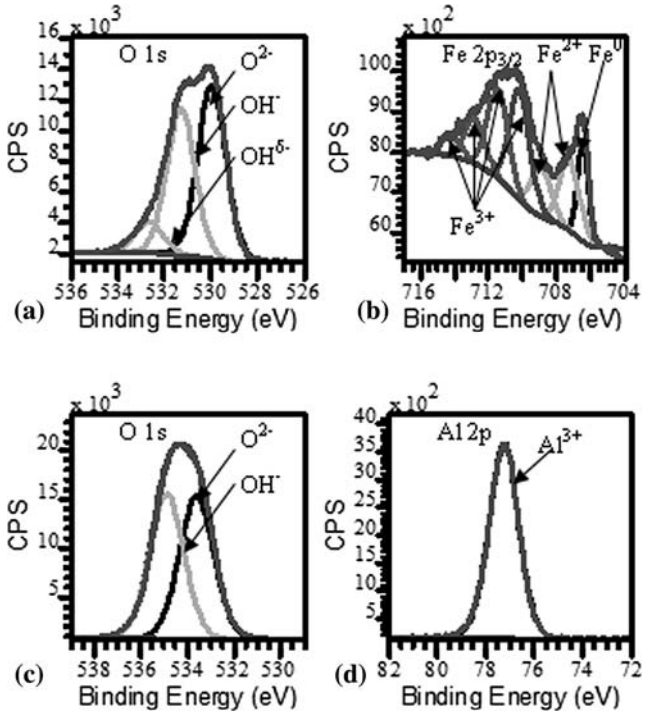

Fig. 6 Narrow scan of the SS_B (a) O 1s, (b) Fe $2p_{3/2}$, and of the Al_B (c) O 1s and (d) Al 2p

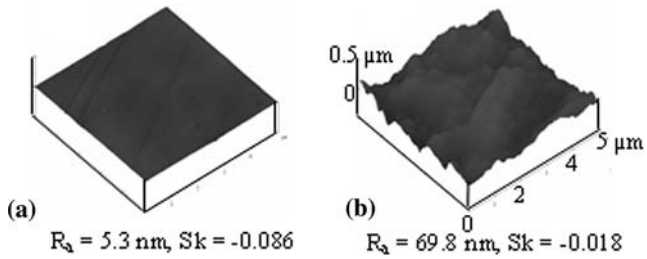

Fig. 7 Surface topologies of the (a) SS_B, and (b) Al_B

substrates (Fig. 7). The surface roughness which was evaluated by two parameters: the average surface roughness (R_a) and skewness (S_k) were examined by atomic force microscope (AFM, NanoScope IIIa) on a scan size of 5 µm. Both surfaces had a similar negative value of S_k, indicating that the surface had more valleys than peaks. However, there was a significant difference in R_a value between two surfaces. It was expected that the larger value of R_a in Al_B substrate compared to SS_B substrate was due to the formation of a thicker oxide/oxyhydroxide layer on the surface.

The significant variations in oxide/oxyhydroxide proportions and thicknesses on SS_B and Al_B surface explain the obvious difference in splat formation between these substrates. It was found from our previous study that the oxyhydroxide readily converted to oxide and released water with the input of heat (Ref 14). When the molten droplet impacts the substrate at high temperature, heat is conducted from the splat to the substrate, resulting in an increase of substrate surface temperature. The dehydration of oxyhydroxide to oxide occurs, $2OOH \rightarrow 2O^{2-} + H_2O$, releasing water vapor, which inhibits the adhesion of impinging splats. The thicker the oxyhydroxide layer was on the surface, the greater the volume of water vapor released and the fewer splats formed. Thus, a high splat density was observed on SS_B surface with the relatively thin surface oxyhydroxide layer on the surface. In contrast, a complete absence of splats on Al_B substrate related to the thick layer of oxyhydroxide on the surface. In addition, the thick layer of formed oxide may decrease the heat transfer from the splat to the substrate due to lower thermal diffusivity compared to that of substrate metal. As a result, the splat was in liquid state long enough to be fragmented and splashed. Thus, it appears that both desorption of large amount of water vapor at high temperature and thick layer of oxide/oxyhydroxide reduced the wettability of the substrate and impede the spreading and adhesion of the splat.

4.2 Numerical Modeling

The impact of a NiCr splat on stainless steel and aluminum substrates was simulated using a free surface model with heat transfer and solidification. It is

well-known that the solidification and the spreading process of molten splat depended strongly on the thermal contact resistance between the splat and the substrate surface (Ref 1, 37). Thermal contact is a complex function of variety parameters: substrate surface conditions, spraying conditions, and the extent of contact at the substrate-splat interface. In addition, thermal contact resistance varies with time and position along the interface. Thus, to measure a real value of thermal contact resistance for a micro-sized droplet is impossible. Instead, a constant value of thermal contact resistance is commonly used in numerical modeling of splat solidification and spreading process. The thermal contact resistance was determined by selecting the value which gave the best agreement between measurement and numerical results. McDonald et al. (Ref 38) and Dhiman et al. (Ref 39) observed that a round disk splat was obtained when nickel or molybdenum particle was plasma-sprayed on stainless steel or inconel substrates. In these cases, the thermal contact resistance was reported to have an order of magnitude of 10^{-6} W^{-1} m^2 K. In addition, reported values of thermal contact resistance range from 10^{-8} to 10^{-5} W^{-1} m^2 K for different cases from good contact to poor contact between the splat and the substrate (Ref 13, 19, 37, 40). The experimental results show a very good contact between the splat and the substrate with evidence of substrate melting. Thus, in our study, the thermal contact resistance of 10^{-8} W^{-1} m^2 K was chosen to examine the splat morphology, pore formation, and the ability of substrate melting. The properties of nickel were used in the model due to the lack of physical properties of NiCr alloy.

Figure 8 shows the sequence of the simulation of a 20 μm diameter nickel splat with the initial temperature of 2527 °C and velocity of 130 m s^{-1} onto the stainless steel substrate held at room temperature. The time measured from the moment of impact is indicated next to each frame. Immediately after impact, the droplet spread out in the radial direction to form a splat. Because the temperature of the underside of the splat decreased to below the melting point of nickel (Fig. 9), a thin layer of solid was formed. The upper liquid portion continued to deform and to flow over the solidified layer and spread out. However, due to a low value of thermal diffusivity of stainless steel substrate, heat transfer from the splat to the bulk substrate was delayed. Heat from the splat body reheated the splat underside, resulting in re-melting and re-freezing phenomena of the splat underside. As can be seen in Fig. 9, the splat underside at the distance of 5 μm from the center of the splat was in liquid form during a period from 0.05 to 0.44 μs. The splat was in liquid form even further toward the edge of the splat, but solidified faster than the locations near the splat center. Due to the differing velocities between the liquid and solid portions of the splat and the inertia force, the liquid portion detached to form a ring around the disk splat of a diameter of ~44 μm (Fig. 8a). It was also found that the solidification started from the periphery and advanced to the center of the splat, leads to the obstruction of splat flow, causing the thicker part at the edge (Fig. 8b). The splat thickness ranged from 0.7 to 2 μm.

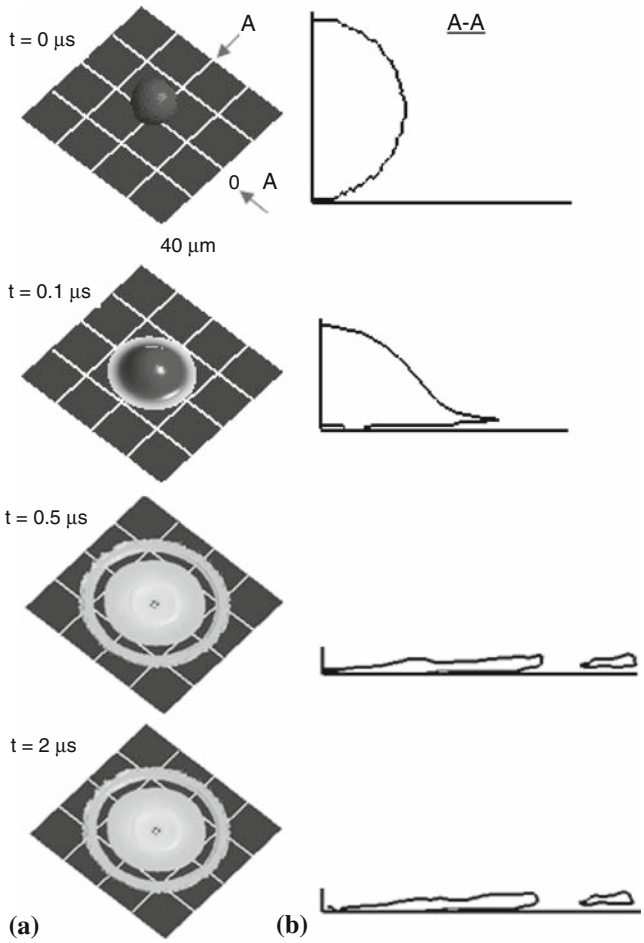

Fig. 8 (a) The sequence of the numerical simulation of a 20 μm diameter nickel splat at 2527 °C with a velocity of 130 m s^{-1} onto the stainless steel substrate at 25 °C with thermal contact resistance of 10^{-8} W^{-1} m^2 K. (b) A schematic diagram of a half cross section of a splat

It was observed from the half cross section of the splat (Fig. 8b) that a central pore was formed in the early stages of the splat spreading. The formation of this central pore is expected due to the change of the surface curvature of the droplet. When the droplet hits the substrate, a high pressure builds at the point of contact. Thus, the normal pressure gradient from the contact point toward the free surface of droplet was positive, resulting in a concave curvature. A bubble then risen up through the liquid film and then broke through the free surface to form the micro-pore at the center of the splat. On this basis, a micro-pore with a diameter of ~1.5 μm was formed. It was also observed that a gas cavity was formed between the splat and the substrate.

Stainless steel has a very low value of thermal diffusivity (5×10^{-6} m^2 s^{-1}), thus most of the heat is retained at the surface: this retards the conduction of the heat front to the bulk. The substrate surface was heated from the impacting splat at sufficiently high temperature for sufficient time, resulting in substrate melting phenomena,

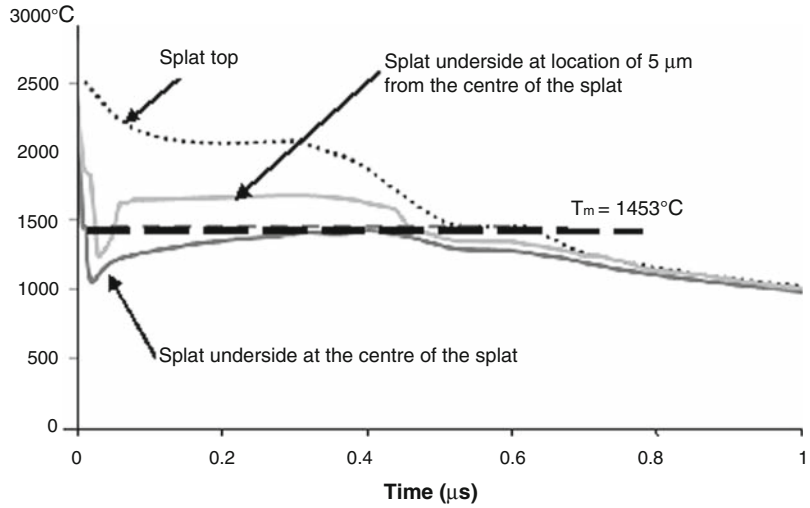

Fig. 9 Temperature distributions of the splat top (1 μm above the impact point) and the splat underside at different locations

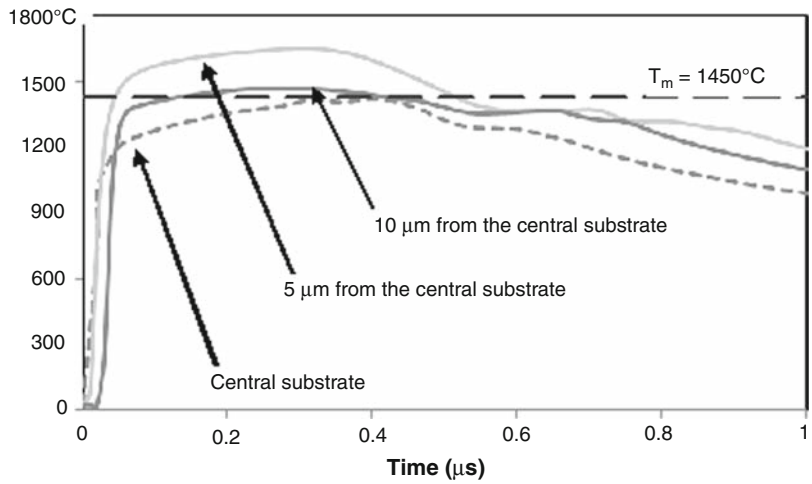

Fig. 10 Temperature distribution of the substrate surface at different locations

where its temperature reaches the equilibrium melting temperature of the stainless steel. Due to the formation of the micro-pore at the center of the splat, the splat-substrate interface changes from one in contact to one in non-contact. As a result, the temperature at the center of the splat is no longer highest. The distribution of substrate surface temperature at the center, and at locations of 5 and 10 μm, as shown in Fig. 10, suggests that the substrate melting occurred at locations just outside of the center of the splat in the early state of the splat spreading. Once the substrate melts, a thin layer of liquid substrate was pushed ahead of the interface toward the NiCr splat, which was still in liquid state at this moment, in order to establish an equal distribution of internal energy. Examination the temperature distribution of the substrate surface revealed that substrate melting should occur within a radius of 15 μm from the splat center. However, experiments show few melting locations even further this area toward the edge of the splat. The model assumes high level of contact that is less than perfect contact. However, perfect contact might occur at specific locations near the edge of the splat, then substrate melting can occur at these locations as empirical observation

4.2.1 Effect of Surface Oxide Layer on Splat Morphologies. The experimental results suggested that the absence of splat formation on boiled aluminum substrate is either due to the effect of thick oxide/oxyhydroxide layer and/or gas release on the substrate surface. To evaluate the effect of oxide layer or gas release on splat morphology, each factor has been separately included in the model. Firstly, a 300 nm thick layer of aluminum oxide on the substrate surface was included in the model. In this case, the model included three domains which represented for splat, oxide layer, and substrate (Fig. 1b). The mass,

momentum, and heat conservations in droplet are unchanged. The heat equation for the oxide layer is written as follows:

$$\frac{\partial T_{ox}}{\partial t} = \alpha_{ox}\nabla^2 T_{ox} \quad \text{(Eq 11)}$$

In this case, thermal contact resistance (R_c) is accounted for discontinuity at the interface between the droplet and oxide layer:

$$\frac{1}{R_c}(T - T_{ox}) = k\frac{\partial T}{\partial x} \quad \text{(Eq 12)}$$

A conservative interface flux at the oxide-substrate interface:

$$k_{sub}\frac{\partial T_{sub}}{\partial x} = k_{ox}\frac{\partial T_{ox}}{\partial x} \quad \text{(Eq 13)}$$

The mass, momentum, and heat equations of droplet, oxide layer, and substrate were solved with the physical properties of aluminum oxide in Table 1. The thermal contact resistance was kept constant at 10^{-8} W^{-1} m^2 K. A mesh size of 100 nm was applied for the oxide domain. Other settings of the mesh size for splat and substrate domains were unchanged. Figure 11(a) shows the splat shape and cross section at 2 μs for the case of 300 nm of aluminum oxide on the aluminum substrate. The numerical results show that the splat spread out to a maximum extent, ruptured, and left the disk splat surrounded by a ring. The maximum temperature of the substrate surface (1500 °C), as can be seen in Fig. 11(b), was well below melting point of the aluminum oxide (2300 °C), suggesting that substrate melting did not occur in this case.

4.2.2 Effect of Gas Release on Splat Morphologies. There was no significant change in the splat shape between the case with a 300 nm thick of oxide layer (Fig. 11a) and the case without oxide layer on the substrate (Fig. 8). This suggests that the oxide thickness (up to 300 nm) is not a dominating factor contributing to the change of splat morphology and the absence of splat on boiled aluminum. The remaining factor to be examined is the effect of water release from the dehydration of aluminum oxyhydroxide to oxide. If the desorption of water occurs in the early stage of the splat spreading process, the flow of water vapor will alter the flow and the spreading of the droplet. Thus, the assumption of laminar flow of the droplet is no longer applicable. In addition, a fluid model is required, which included the flows of water release in both the droplet and the ambient atmosphere. An evaporation model of released water and mass transfer between the splat and the water release are also required. A complete solution is extremely challenging to solve. However, the most probable hypothesis appears to be that the insulating layer of released water inhibits heat transfer from the splat to the substrate. The droplet was in a liquid state long enough, and then spread to form a thin layer on the substrate surface. Larger volumes of released water, as is the case with hydrothermally treated Al_B surfaces generates high vapor pressure which readily explodes the molten thin layer of splat, resulting in the fragmentation of the splat and forming small residues and droplets landed on the substrate surface as observed.

5. Conclusions

The impact of plasma-sprayed NiCr alloy particles at room temperature on stainless steel and aluminum substrates with different oxide/oxyhydroxide compositions and thickness has been studied. It was found that a significant number of splats with high percentage of disk-shaped and donut splats were formed on boiled stainless steel substrate. In contrast, there was no splat formation on boiled aluminum substrate. Splats were also not found on boiled aluminum substrate with variations of spraying conditions, surface roughness and particle properties. These experimental results suggest that the significant difference in splat formation on boiled stainless steel and boiled aluminum surface is definitely due to the substrate surface chemistry, in particular the oxyhydroxide proportion and thickness. FIB cross section studies of disk splats on boiled stainless steel substrate revealed NiCr splats adhered well in some locations with the possibility of substrate melting. Pores with different sizes were observed at some locations along the splat-substrate interface.

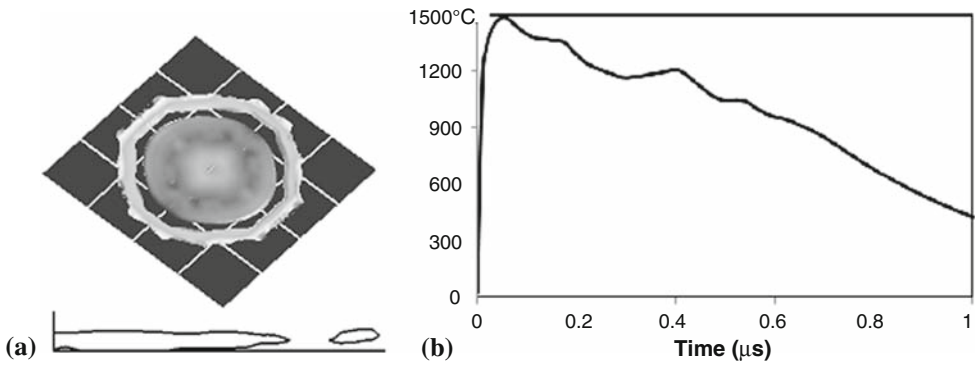

Fig. 11 (a) Splat shape of Ni on aluminum substrate at 2 μs with taking into account the effect of 300 nm thick of the oxide layer, and (b) temperature distribution of substrate surface

Central pore with various sizes was often found in disk splat and donut splat.

A three-dimensional numerical model was developed to simulate the impact of a molten nickel splat onto the substrate. The simulation illustrated good agreements with the experiments in the splat morphology, the formation of the pores, the delamination of the splat at the periphery, and the specific locations of substrate melting. The effect of oxide layer on the splat morphology was also included in the model. It was found that the splat morphology was not influenced by the thickness of the oxide layer on the substrate surface. From the experimental and simulation results, it was suggested that the complete absence of the splat on boiled aluminum surface was due to the thick layer of oxyhydroxide at the outer substrate surface. When a molten particle impacts the boiled aluminum surface at high temperature, the dehydration of oxyhydroxide to oxide occurs and releases a large volume of water vapor. This vapor layer inhibits the heat conduction from the particle to the substrate. As a result, the particle remains in the liquid state long enough. Then, the flow of water release with high pressure readily explodes the liquid film. The liquid film disintegrates, resulting in the formation of small droplets and residues on the substrate surface.

Acknowledgments

The author would like to acknowledge Tertiary Education Commission of New Zealand for Top Achiever Doctoral scholarship.

References

1. S. Chandra and P. Fauchais, Formation of Solid Splats during Thermal Spray Deposition, *J. Thermal Spray Technol.*, 2009, **18**(2), p 148-180
2. P. Fauchais, M. Fukumoto, A. Vardella, and M. Vardella, Knowledge Concerning Splat Formation: An Invited Review, *J. Thermal Spray Technol.*, 2004, **13**(3), p 337-360
3. S. Dallaire, Influence of Temperature on the Bonding Mechanism of Plasma-Sprayed Coatings, *Thin Solid Films*, 1982, **95**(3), p 237-244
4. R.C. Dykhuizen, Review of Impact and Solidification of Molten Thermal Spray Droplets, *J. Thermal Spray Technol.*, 1994, **3**(4), p 351-361
5. M. Fukumoto, H. Nagai, and T. Yasui, Influence of Surface Character Change of Substrate due to Heating on Flattening Behavior of Thermal Spray Particle, *J. Thermal Spray Technol.*, 2006, **15**(4), p 759-764
6. M. Fukumoto, I. Ohgitani, M. Shiiba, and T. Yasui, Effect of Substrate Surface Change by Heating on Transition in Flattening Behavior of Thermal Sprayed Particles, *Mater. Trans.*, 2004, **45**(6), p 1869-1873
7. X. Jiang, W. Yuepeng, H. Herbert, and S. Sanjay, Role of Condensates and Adsorbates on Substrate Surface on Fragmentation of Impinging Molten Droplets During Thermal Spray, *Thin Solid Films*, 2001, **385**(1-2), p 132-141
8. C.J. Li and J.L. Li, Evaporated-Gas-Induced Splashing Model for Splat Formation During Plasma Spraying, *Surf. Coat. Technol.*, 2003, **184**(1), p 13-23
9. M. Fukumoto and Y. Huang, Flattening Mechanism in Thermal Sprayed Ni Particles Impinging on Flat Substrate Surface, *J. Thermal Spray Technol.*, 1999, **8**(3), p 427-432
10. M. Fukumoto, T. Yamaguchi, M. Yamada, and T. Yasui, Splash Splat to Disk Splat Transition Behavior in Plasma-Sprayed Metallic Materials, *J. Thermal Spray Technol.*, 2007, **16**(5-6), p 905-912
11. A. McDonald, M. Lamontagne, C. Moreau, and S. Chandra, Impact of Plasma-Sprayed Metal Particles on Hot and Cold Glass Surfaces, *Thin Solid Films*, 2006, **514**(4), p 212-222
12. V. Pershin, M. Lufitha, S. Chandra, and J. Mostaghimi, Effect of Substrate Temperature on Adhesion Strength of Plasma-Sprayed Nickel Coatings, *J. Thermal Spray Technol.*, 2003, **12**, p 370-376
13. M. Pasandideh-Fard, V. Pershin, S. Chandra, and J. Mostaghimi, Splat Shapes in a Thermal Spray Coating Process: Simulations and Experiments, *J. Thermal Spray Technol.*, 2001, **11**, p 206-217
14. A.T.T. Tran, M.M. Hyland, T. Qiu, B. Withy, and B.J. James, Effects of Surface Chemistry on Splat Formation during Plasma Spraying, *J. Thermal Spray Technol.*, 2008, **17**(5-6), p 637-645
15. J. Mostaghimi, S. Chandra, R. Ghafouri-Azar, and A. Dolatabadi, Modeling Thermal Spray Coating Processes: A Powerful Tool in Design and Optimization, *Surf. Coat. Technol.*, 2003, **163-164**, p 1-11
16. M.F. Bahbou and P. Nylen, On-line Measurement of Plasma-Sprayed Ni-Particles During Impact on a Ti-Surface: Influence of Surface Oxidation, *J. Thermal Spray Technol.*, 2007, **16**(4), p 506-511
17. M. Pasandideh-Fard, S. Chandra, and J. Mostaghimi, A Three-Dimensional Model of Droplet Impact and Solidification, *Int. J. Heat Mass Transfer*, 2002, **45**, p 2229-2242
18. A. McDonald, M. Xue, S. Chandra, J. Mostaghimi, and C. Moreau, Modeling Fragmentation of Plasma-Sprayed Particles Impacting on a Solid Surface at Room Temperature, *Comptes Rendus Mecanique*, 2007, **335**, p 351-356
19. H.R. Salimijazi, M. Raessi, J. Mostaghimi, and T.W. Coyle, Study of Solidification Behavior and Splat Morphology of Vacuum Plasma Sprayed Ti Alloy by Computational Modeling and Experimental Results, *Surf. Coat. Technol.*, 2007, **201**(18), p 7924-7931
20. M. Bussmann, J. Mostaghimi, and S. Chandra, On a Three-Dimensional Volume Tracking Model of Droplet Impact, *Phys. Fluids*, 1999, **11**, p 1406-1417
21. M. Bussmann, S. Chandra, and J. Mostaghimi, Modeling the Splash of a Droplet Impacting a Solid Surface, *Phys. Fluids*, 2000, **12**, p 3121-3132
22. J. Cedelle, M. Vardelle, and P. Fauchais, Influence of Stainless Steel Substrate Preheating on Surface Topography and on Millimeter- and Micrometer-sized Splat Formation, *Surf. Coat. Technol.*, 2006, **201**, p 1373-1382
23. A. McDonald, C. Moreau, and S. Chandra, Effect of Substrate Oxidation on Spreading of Plasma-Sprayed Nickel on Stainless Steel, *Surf. Coat. Technol.*, 2007, **202**, p 23-33
24. A. McDonald, S. Chandra, and C. Moreau, Photographing Impact of Plasma-Sprayed Particles on Rough Substrates, *J. Mater. Sci.*, 2008, **43**, p 4631-4643
25. H.B. Parizi, L. Rosenzweig, J. Mostaghimi, S. Chandra, T. Coyle, H. Salimi, L. Pershin, A. McDonald, and C. Moreau, Numerical Simulation of Droplet Impact on Patterned Surfaces, *J. Thermal Spray Technol.*, 2007, **16**(5-6), p 713-721
26. J.U. Brackbill, D.B. Kothe, and C. Zemach, A Continuum Method for Modeling Surface Tension, *J. Comput. Phys.*, 1992, **100**, p 335-354
27. S.-P. Wang, G.-X. Wang, and E.F. Matthys, Melting and Resolidification of a Substrate in Contact with a Molten Metal: Operational Maps, *Int. J. Heat Mass Transfer*, 1998, **41**(10), p 1177-1188
28. W.D. Bennon and F.P. Incropera, A Continuum Model for Momentum, Heat and Species Transport in Binary Solid-Liquid Phase Change Systems—I. Model Formulation, *Int. J. Heat Mass Transfer*, 1987, **30**(10), p 2161-2170
29. C. Prakash and V. Voller, On the Numerical Solution of Continuum Mixture Model Equations Describing Binary Solid-Liquid Phase Change, *Numer. Heat Transfer B*, 1989, **15**(2), p 171-189
30. C.W. Hirt and B.D. Nichols, Volume of Fluid (VOF) Methods for the Dynamics of Free Boundaries, *J. Comput. Phys.*, 1981, **39**, p 201-225

31. H.K. Versteeg and W. Malalasekera, *An Introduction to Computational Fluid Dynamics: The Finite Volume Method*, 2nd ed., Prentice-Hall, Englewood Cliffs, NJ, 2007
32. Ansys Inc., Ansys CFX Documentation, 2007, USA
33. S. Brossard, P.R. Munroe, A.T.T. Tran, and M.M. Hyland, Study of the Splat-Substrate Interface for a NiCr Coating Plasma Sprayed on to Polished Aluminum and Stainless Steel Substrates, in *International Thermal Spray Coating: Expanding Thermal Spray Performance to New Markets and Applications*, 2009, Las Vegas, US
34. W.J. Trompetter, *Splat-Substrate Interactions in High Velocity Thermal Spray Coatings*, PhD thesis, University of Auckland, 2008
35. A.P. Grosvenor, B.A. Kobe, and N.S. McIntyre, Examination of the Oxidation of Iron by Oxygen using X-ray Photoelectron Spectroscopy and QUASES, *Surf. Sci.*, 2004, **565**(2-3), p 151-162
36. M.R. Alexander, G.E. Thompson, and G. Beamson, Characterization of the Oxide/Hydroxide Surface of Aluminum Using X-ray Photoelectron Spectroscopy: A Procedure for Curve Fitting the O 1 s Core Level, *Surf. Interface Anal.*, 2000, **29**(7), p 468-477
37. R. Dhiman and S. Chandra, Freezing-Induced Splashing During Impact of Molten Metal Droplets with High Weber Numbers, *Int. J. Heat Mass Transfer*, 2005, **48**(25-26), p 5625-5638
38. A. McDonald, C. Moreau, and S. Chandra, Thermal Contact Resistance Between Plasma-Sprayed Particles and Flat Surfaces, *Int. J. Heat Mass Transfer*, 2007, **50**, p 1737-1749
39. R. Dhiman, A.G. McDonald, and S. Chandra, Predicting Splat Morphology in a Thermal Spray Process, *Surf. Coat. Technol.*, 2007, **201**, p 7789-7801
40. A. McDonald, C. Moreau, and S. Chandra, Thermal Contact Resistance Between Plasma-Sprayed Particles and Flat Surfaces, *Int. J. Heat Mass Transfer*, 2006, **50**, p 1737-1749
41. D.R. Lide, *CRC Handbook of Chemistry and Physics, 86th Edition (CDROM Version 2006)*, Taylor and Francis, Boca Raton, FL, 2006